INDONESIAN JOURNAL ON GEOSCIENCE
Geological Agency
Ministry of Energy and Mineral Resources

Journal homepage: https://ijog.geologi.esdm.go.id
ISSN 2355-9314, e-ISSN 2355-9306

Enhancing Seismic Hazard Preparation in Lampung, Sumatra: Improved Magnitude Conversion, Seismicity Smoothing, and Area Source Modeling

Rizki Wulandari[1,2], Yudha Styawan[1,2], and Chung-Han Chan[1,3,4]

[1]Department of Geophysical Engineering, Sumatra Institute of Technology, Lampung, Indonesia
[2]The Sumatra Earthquake and Tsunami Mitigation Center, Sumatra Institute of Technology, Lampung, Indonesia
[3]Department of Earth Sciences, National Central University, Taoyuan City, Taiwan
[4]Earthquake-Disaster & Risk Evaluation and Management (E-DREaM) Center, National Central University, Taoyuan City, Taiwan

Corresponding author: rizki.wulandari@tg.itera.ac.id
Manuscript received: November, 05, 2024; revised: August, 12, 2025;
approved: February, 17, 2026; available online: June, 22, 2026

Abstract – This work improves seismic hazard evaluation for the Lampung region in Sumatra by tackling the precision in magnitude conversion, attenuation of seismicity, and area-source modelling. Considering the variety magnitude. The magnitude conversion equations were initially validated using scales from historical earthquake data. And, if required, enhanced to guarantee their dependability for the area. Utilizing maximum likelihood estimation Maximum Likelihood Estimation (MLE) and ordinary. Ordinary least squares (OLS) regression was employed to compute parameters for frequency-magnitude distributions. Facilitating a comprehensive comparison that acknowledges OLS's sporadically superior alignment with observed data. Gaussian distribution smoothing was utilized diverse bandwidths (25, 50, 75, and 100 km) to illustrate spatial seismicity patterns, disclosing a distance of 50 kilometers. Bandwidth provides the most consistent model performance, especially in terms of accuracy in the Molchan illustration. The area skill score (ASS) validates the superior forecasting capacity of the smoothed seismicity models. Using bandwidths of 25, 50, and 75 kilometers producing competitive outcomes. Furthermore, the region was partitioned into discrete seismic zones predicated on fault characteristics and seismicity density, further augmenting localized hazard assessments. This is polished. multi-method approach encompassing magnitude conversion, spatial smoothing, and area-specific analysis. Modelling offers a comprehensive framework for seismic hazard preparedness in Lampung, providing useful insights for infrastructure strategic planning and disaster mitigation.

Keywords: Magnitude conversion, seismic hazard, seismicity smoothing, area source model, Lampung, Sumatra

How to cite this article:
Wulandari, R. and Styawan, Y., and Chan, C.H., 2026. Enhancing Seismic Hazard Preparation in Lampung, Sumatra: Improved Magnitude Conversion, Seismicity Smoothing, and Area-Source Modeling. *Indonesian Journal on Geoscience*, 13 (2), p.221-241. DOI: 10.17014/ijog.13.2.221-241

Introduction

Background

Lampung, located at the southern tip of Sumatra, is positioned as a crucial economic link between Sumatra and Java, two of Indonesia's most vital regions in terms of population density and economic activity (Hu *et al*., 2026). This strategic location makes Lampung essential for regional development, but it also faces various natural hazards, particularly seismic and volcanic activity. Lampung faces various natural hazards, particularly seismic events and volcanic activity. The region is highly seismically active,

primarily because of the transition zone that exists between the normal subduction beneath Java and the oblique subduction beneath Sumatra, where the Indo-Australian Plate converges with the Eurasian Plate (Collings *et al*., 2013; McCaffrey, 2009). This tectonic setting not only results in convergent plate boundaries but also features shallow active faults within the region (Bellier *et al*., 1997; Bradley *et al*., 2017; Sieh and Natawidjaja, 2000). Given this tectonic framework, the two principal seismic sources influence the Lampung region: the Sunda Megathrust to the south and the Great Sumatran Fault (GSF) to the west, with each contributing to the region's overall tectonic complexity and seismic hazard potential. Historically, several large earthquakes have occurred in the area shown in Figure 1 (last accessed on 25th September 2024, https://www.

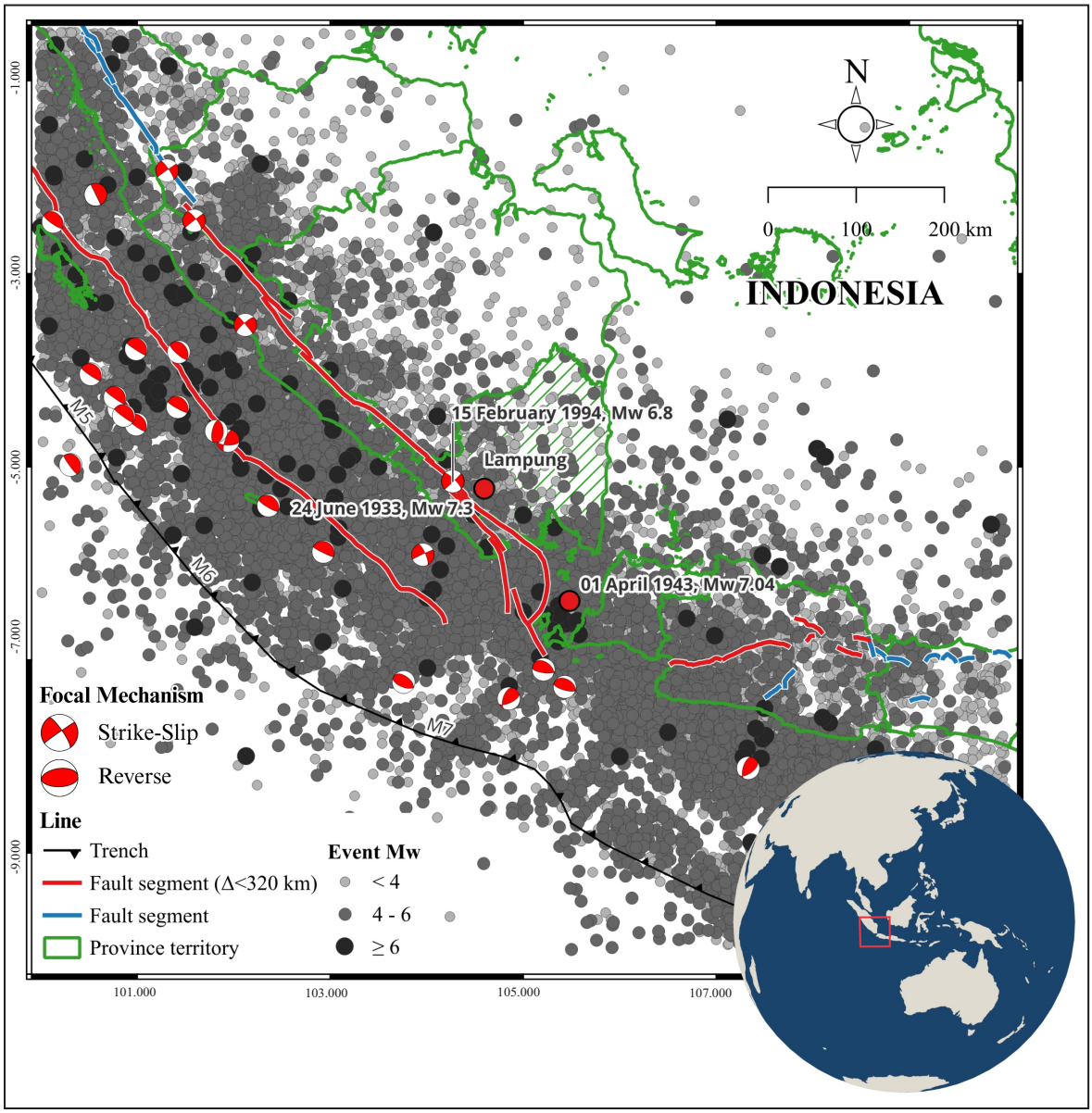

Figure 1. Seismicity data and historical earthquakes $M_w \geq 6.5$ including their focal mechanisms after conversion (Willemann and Storchak, 2001). earthquake epicenters (1964-2024) are shown by circles scaled to magnitude, with color classifications for M_w 4,4-6, and ≥6. Red circles represent historical earthquakes discussed in the background section for which focal mechanisms are unavailable. Red lines denote active fault segments (<320 km), blue lines indicate other mapped fault segments (Irsyam *et al*., 2017), and the black line marks the subduction trench. The hatched area delineates Lampung Province boundary. Major historical events are annotated with their occurrence dates and magnitudes.

isc.ac.uk/iscbulletin/search/). On June 24th, 1933, a magnitude 7.5 M earthquake struck at a depth of 20 km. The earthquake occurred at a depth of 20 km, with the majority of the shaking registering a modified Mercalli intensity (MMI) VII, which affected areas as far away as Java and even Singapore. This event was likely associated with shallow crustal faulting in the onshore segment of the Great Sumatran Fault system, reflecting strike-slip motion along the fault zone. Another significant event occurred in February 1994, when a magnitude of a 6.9 earthquake struck at a depth of 23.1 km, which also appears to have originated from the same fault system near the 1933 epicentral area, suggesting repeated activity along a similar crustal structure. Additionally, on April 1st, 1943, a magnitude 7.0 an earthquake occurred at a depth of 35 km in the Sunda Strait, which is interpreted to be related to slip on the deeper portion of the Sunda subduction interface, producing shaking measured at modified Mercalli intensity (MMI) VI, affecting Lampung and its surrounding areas.

Given the region's vulnerability, a detailed and high-resolution seismic hazard assessment is necessary to mitigate potential disasters. However, the current seismic hazard models for Lampung, Sumatra, and even Indonesia have a certain constrains (e.g., Irsyam *et al*., 2020; Petersen *et al*., 2004; Triyoso *et al*., 2020; Triyoso and Sahara, 2021; Haifani *et al*., 2026; Rasimeng *et al*., 2022), particularly in the application of area source modeling and seismicity smoothing techniques. These methodologies are essential for accurate hazard forecasts as they account for the spatial distribution of earthquake events and improve hazard resolution, crucial for regions like Lampung, which face a complex tectonic setting.

This study aims to bridge these gaps by first converting existing magnitude catalogues, which ensures that the seismicity data is uniform and reliable for further analysis. Earthquake magnitudes are often reported using different scales (e.g., moment magnitude M_w, local magnitude M_l, surface-wave magnitude M_s, etc.), and these scales measure different aspects of an earthquake's energy or effects. Since probabilistic seismic hazard assessment (PSHA) requires a uniform dataset to assess seismic hazards, converting magnitudes to a single, consistent scale—typically the moment magnitude M_w - ensures that all earthquake data can be directly compared and properly integrated into the hazard model (e.g., Irsyam *et al*., 2017). Moment magnitude (M_w) is a commonly used scale for measuring seismic size that was developed prior to the availability of modern seismological techniques (Hanks and Kanamori, 1979). Unlike other scales, such as local magnitude (M_l) or surface-wave magnitude (M_s), which can saturate and underestimate the size of larger earthquakes (aroundM6 - 6.5 for M_l and ~M7.5 for M_s. Unlike these scales, M_w accurately represents the total energy released during an earthquake, making it ideal for use in seismic hazard assessments.

In this study, after obtaining reliable catalogues for further analysis, we propose an earthquake forecasting approach specifically designed for Lampung, integrating seismicity smoothing techniques and area source modeling to enhance the spatial and temporal resolution of earthquake sources. Seismicity smoothing is then applied to obtain high-resolution seismicity rates, offering a more precise representation of seismicity rates in the region as proposed by Frankel (1995). In addition, the area source model, which segments regions into seismic zones (Wiemer *et al*., 2009), is developed to complement the smoothing technique (e.g., Xhafaj *et al*., 2024). These models are validated using the Molchan diagram, a statistical tool that evaluates the performance of earthquake forecasting models (Kagan and Jackson, 1994; Molchan, 1990; Zechar and Jordan, 2008).

The outcomes of this research have significant implications for seismic hazard preparation, particularly concerning shallow seismic sources. Increasing awareness of seismic sources in Lampung can improve disaster readiness across various sectors, from infrastructure development

to community safety planning. As a vital region for economic growth, strengthening resilience against seismic hazards is crucial not only for safeguarding local populations but also for ensuring national economic stability.

Tectonic Settings

Lampung is situated at the transition between the normal subduction beneath Java and the oblique subduction beneath Sumatra (Figure 1), making it a key area for studying complex tectonic interactions. Figure 1 illustrates the historical seismicity, mapped faults, and segmentation of the Sunda Megathrust considered in this study. The region is primarily shaped by the oblique subduction of the Indo-Australian Plate beneath the Eurasian Plate along the Sunda megathrust. This oblique convergence results in both compressional and strike-slip deformation, contributing to the region's high seismicity.

The Sunda megathrust is segmented along its length, with distinct seismic behavior associated with each segment. The segmentation was defined by rupture area of the largest historical earthquake (e.g., Haridhi *et al*., 2018; McCaffrey, 2009; Natawidjaja *et al*., 2006; Pesicek *et al*., 2008; Qiu and Chan, 2019; Singh *et al*., 2008; Subarya *et al*., 2006). This tectonic complexity is further compounded by the presence of the Great Sumatran Fault (GSF), an active strike-slip fault system that runs along the spine of Sumatra, accommodating significant lateral displacement. For seismic hazard assessment, international guidelines recommend a source-to-site minimum radius of 320 km to account for significant seismic sources around the site (USNRC, 2007). Although originally developed for nuclear power plant assessments, this radius has been widely adopted in regional hazard studies where both crustal and subduction sources contribute to seismic hazard assessment (e.g., Mandal *et al*., 2013; Lamichhane *et al*., 2025). Its application to Lampung is appropriate given the region's proximity to the Sunda Megathrust and active fault systems. Accordingly, we selected seismic sources within this radius, as illustrated in Figure 1.

Methods and Materials

Materials

In this study, seismicity data were sourced from the International Seismological Centre (ISC) Bulletin, covering the period from 1900 to 2024 (Willemann and Storchak, 2001). The ISC catalogue is compiled from multiple seismic agencies worldwide, including global and regional networks that contribute earthquake parameters such as location, magnitude, depth, and focal mechanism solutions. These agencies contribute data on event location, magnitude, depth, and focal mechanisms, which are further reviewed and vetted by the ISC to maintain high-quality standards. Often, different agencies report various types of magnitudes for the same event, such as surface-wave magnitude (M_s), moment magnitude (M_w), narrow band body wave magnitude (mb), boardband body wave magnitude (mB), local magnitude (M_L), local vertical magnitude (M_{LV}), summary magnitude (M), which are all included in the catalogue.

M_s measures the amplitude of Rayleigh surface waves, typically at a period of around 20 seconds. mb is a narrow-band body wave magnitude determined using WWSSN-SP filtered trace. mB also measures body wave amplitudes, but unlike mb, it uses a broader frequency range and longer time windows. M_L refer to the local magnitude, initially developed by Richter (1958) for Southern California. M_{LV} is a local magnitude calculated using the vertical component and adjusted to align with the standard M_L. M is a summary magnitude that represents a weighted average of different magnitude types, aiming to produce the best overall estimate. M_w is based on the relationship between seismic energy and seismic moment. Since it does not saturate for either large or small events, M_w is considered the most reliable scale for conversion to a uniform magnitude, making it ideal for seismic hazard assessments (Baker *et al*., 2022).

An example of the ISC catalogue content used in this study includes detailed earthquake information shown in Table 1. An earthquake in 1943, summarized by three agencies: ISC,

Table 1. Examples of the ISC content catalogue. The available agencies on the other events are variant and different from this table.

Agency	m_b	m_B	M_S	M_L	M_{Lv}	M	M_W
date: 1943-04-01, time: 14:18:17.10, latitude: -6.3894, longitude: 105.4796, depth: 35.0							
ISC	-	-	7.2	-	-	-	-
PAS	-	-	7.0	-	-	-	-
ABE1	-	6.9	7.1	-	-	-	-
date: 2024-07-10, time: 15:32:42, latitude: -5.4, longitude: 100.9, depth: 10.0							
IPGP	-	-	-	-	-	-	5.8
IDC	5.2	-	5.2	4.9	-	-	-
NEIC	-	-	-	-	-	5.4	-
GFZ	6.0	-	-	-	-	5.7	-
date: 1984-01-05, time: 07:43:08.29, latitude: -5.1174, longitude: 102.2559, depth: 31.7							
ISC	5.6	-	5.2	-	-	-	-
DJA	5.6	-		4.5	-	-	-
NEIS	5.4	-	5.1	-	-	-	-
PEK	4.8	-	5.5	-	-	-	-
MOS	5.8	-	5.2	-	-	-	-
GCMT	-	-	-	-	-	-	5.3

ISC* International Seismological Centre (2024)
PAS* California Institute of Technology
ABE1* Abe (1981)
IPGP* Institut de Physique du Globe de Paris
IDC* International Data Centre, CTBTO
NEIC* National Earthquake Information Centre
GFZ* German Research Centre for Geosciences
NEIS* National Earthquake Information Service
PEK* Peking, China
MOS* Geophysical Survey of Russian Academy of Sciences
GCMT* The Global CMT Project
DJA* Badan Meteorologi, Klimatologi dan Geofisika, Indonesia
*directly provided by ISC Bulletin

PAS, and ABE1 which contain mb and M_s with different level. Furthermore, in 2024 was occured earthquake with magnitude summarized by IPGP M_w = 5.8, IDC mB = 5.2; M_{Ls} = 5.2; M_L = 4.9, NEIC M = 5.4, and GFZ mb = 6.0; M = 5.7. All data 24.315 earthquake events, each events contain different magnitude types this range of magnitude types allows for converting to a magnitude scale.

Methods

Improving seismic hazard preparation in Lampung, Sumatra, involves several methodical steps, each critical in ensuring the accuracy and reliability of earthquake data for better hazard assessment. The first component, magnitude conversion, aims to standardize all recorded earthquake magnitudes by converting them to M_w. Moment magnitude is particularly useful because it remains accurate for larger seismic events, unlike other magnitude scales that tend to saturate and underestimate energy release in larger earthquakes. The process begins by gathering earthquake records that have both moment magnitudes and other magnitude types, such as mb, mB, M_s, M_L , M_{Lv}, and M. Using Ordinary Least Squares (OLS) regression, a relationship is established between M_w and each of these other types (Kadirioğlu and Kartal, 2016). After deriving a mathematical expression with an R-squared value as a consideration, this expression is applied to events that lack a recorded moment magnitude, enabling consistent moment magnitude data across the catalog.

To further refine the data, declustering of the earthquake catalog is implemented, with the primary goal of isolating independent seismic events by removing foreshocks and aftershocks. This step is essential because foreshocks and aftershocks are time-dependent and can distort statistical analyses if included indiscriminately. Focusing on events from 1964 onward, the

Gardner and Knopoff (1974) method is used to decluster the dataset. This method identifies and removes dependent seismic events, ensuring a catalog of mainshock events that provides a more reliable basis for seismic hazard assessment.

Smoothing seismicity is the next phase, designed to create a more uniform picture of earthquake occurrence across the study area. The first task is to determine the magnitude of completeness (M_c) over time, from 1964 to 2024, ensuring that only well-documented earthquakes are included in the analysis. Based on the magnitude of completeness, a correction factor (t_f) is calculated (Weichert, 1980). The study area is divided into a grid with intervals of 0.2 x 0.2°. In each cell, earthquake events up to 2014 are counted, and their magnitudes and the year of occurrences are assessed to confirm they meet the M_c threshold and the year of M_c. The counts are then adjusted by t_f, resulting in an estimated rate of events per cell. Earthquake events recorded post-2014 serve as test data in a Molchan diagram, an evaluative tool for predictive accuracy (Molchan, 1991; Molchan and Kagan, 1992). Seismicity smoothing within each cell is conducted using an isotropic Gaussian smoothing kernel (Frankel, 1995), with varying bandwidths, they are 25, 50, 75, and 100.

Another spatial approach is achieved by defining area sources based on seismic activity patterns. To begin with, in the entire study region, *a* and *b* values are calculated using data from events up to 2014, while post-2014 events again serve as test data in the Molchan diagram. Besides, M_c is checked for the entire dataset. Maximum Likelihood Estimation (MLE) and OLS regression methods are compared to estimate the *a* and *b* values, which represent the frequency-magnitude distribution (FMD) characteristics. If necessary, the regression trend can be split into two, with weighting based on data density for each trend segment. The study area is then divided into smaller regions considering factors like slip rates, seismic source types, and event density. Each area is reassessed for the *a* and *b* values, with an option to fix the *b* value at 1- matching the assumed *b* for smoothed seismicity - is evaluated. The M_c for the smaller regions is standardized using the value from the entire study area.

Finally, the Molchan diagram is employed to compare the predictive accuracy of the smoothed area using variant bandwidths and the area source model, providing insights into the reliability of each approach. By calculating the Area Skill Score (ASS) as the area above the Molchan diagram, a quantitative measure of predictive skill is obtained (Zechar and Jordan, 2010). Those calculations are conducted using Python implementing and modifying the particular code from Savran *et al*. (2024). This final step helps determine the most effective model for forecasting and hazard preparation in Lampung.

Result and Analysis

Magnitude Conversion and Seismicity Data

Figure 2a-f presents the linear regression analysis between M_w and various magnitude scales. The red lines represent the best-fit linear relationships, with corresponding regression equations shown in each panel. In addition, the summary of Figure 2 is shown in Table 2. The first panel (Figure 2a) shows a strong linear relationship between M_w and mb. The regression equation M_W = -0.06501 + 1.0198mb indicates a near 1:1 correlation between these two magnitude types, suggesting that mb can be a reliable predictor of M_w with minimal conversion bias. The high clustering of data points around the regression line reinforces the strength of this relationship. For another form of body wave magnitude (mB) in Figure 2b, the relationship with M_w is divided into two magnitude ranges: mB ≤6.5 and mB >6.5. The regression results show that the relationship is weaker for smaller magnitudes, with a slope of 0.81118, while for larger events, the slope increases to 1.2033. This difference implies that mB underestimates M_w at lower magnitudes but becomes more accurate for higher-magnitude events. The M_s shows a segmented relationship with M_w (Figure 2c), similar to mB. For magni-

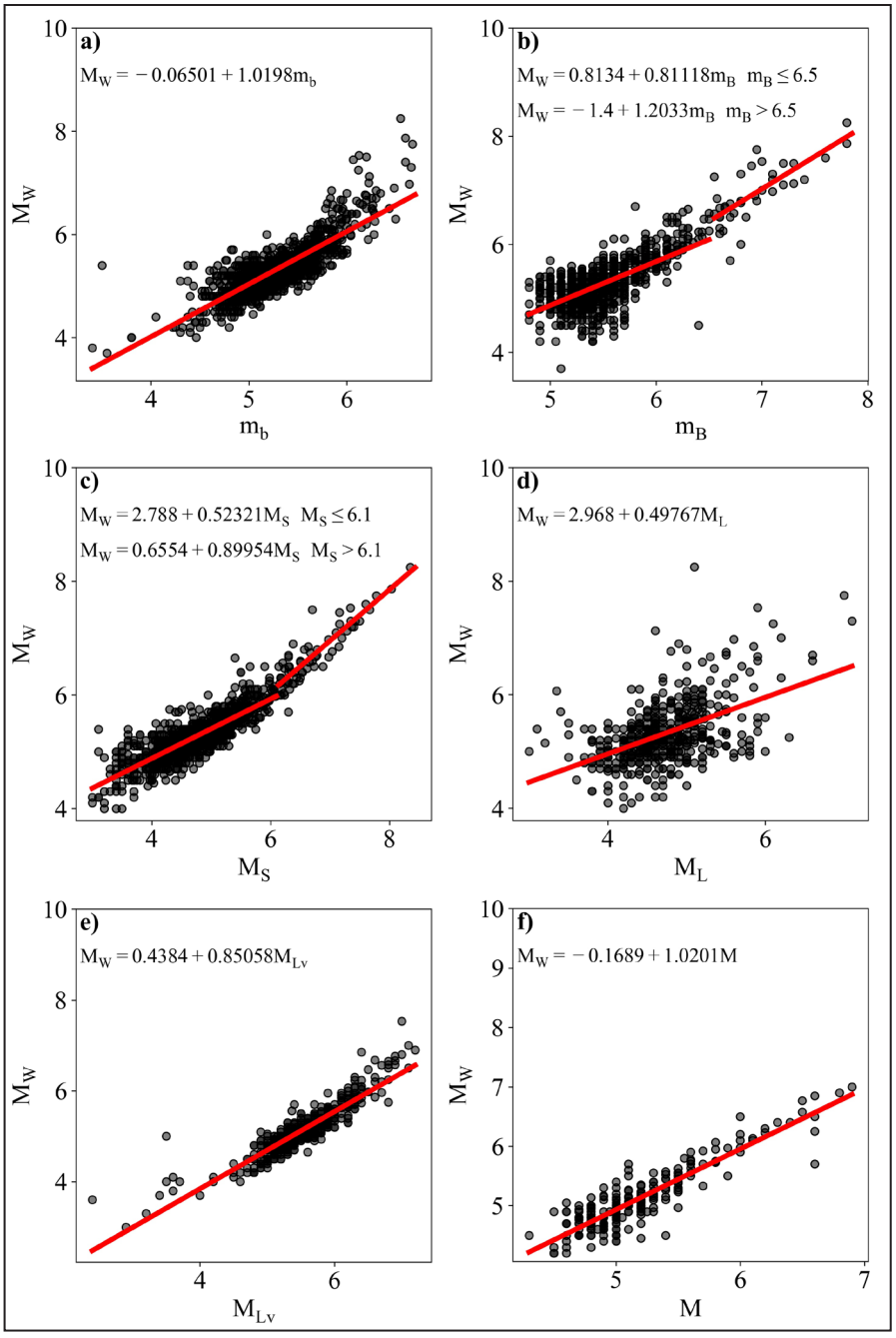

Figure 2. The plot between M_w and other magnitudes. Red lines represent their regressions.

tudes M_s ≤6, the regression slope is relatively low (0.52321), indicating that M_s increases more slowly compared to M_w. However, for larger magnitudes (M_s >6.1), the slope increases to 0.89954, suggesting a stronger correlation. Local magnitude (M_L) shows a weaker linear relationship with M_w compared to the previous magnitude types (Figure 2d). The slope of 0.49767 suggests that M_L generally underestimates M_w, particularly at higher values. For the relationship between M_w and M_{LV} (Figure 2d) shows a moderately strong correlation, with a slope of 0.85058. The final panel (Figure 2f) presents the relationship between M_w and a generic magnitude type M, with a near-perfect slope of 1.0201. The data points show minimal scatter, indicating that M is almost directly comparable to M_w. This panel demonstrates that the generic magnitude M can

Table 2. Relationships between Moment Magnitude (M_w) and Other Magnitude Scales (mb, mB, MS, ML, MLv, M). Each row details the regression equations used to convert various magnitude scales to M_w, along with the respective data range, total number of events, and the coefficient of determination (R^2) for each relationship.

Magnitude	Equation	Data Range	Total of events	R^2
M_W and m_b	$M_W = -0.06501 + 1.0198m_b$	$3.4 \le m_b \le 6.67$	1066	0.680
M_W and m_B	$M_W = 0.8134 + 0.81118m_B$ $m_B \le 6.5$	$4.8 \le m_B \le 6.5$	842	0.423
	$M_W = -1.4 + 1.2033m_B$ $m_B > 6.5$	$6.55 \le m_B \le 7.8$	37	0.566
M_W and M_S	$M_W = 2.788 + 0.52321M_S$ $M_S \le 6.1$	$3.0 \le M_S \le 6.08$	950	0.688
	$M_W = 0.6554 + 0.89954M_S$ $M_S > 6.1$	$6.13 \le M_S \le 8.35$	66	0.814
M_W and M_L	$M_W = 2.968 + 0.49767M_L$	$3.0 \le M_L \le 7.1$	485	0.255
M_W and M_{Lv}	$M_W = 0.4384 + 0.85058M_{Lv}$	$2.4 \le M_{Lv} \le 7.2$	459	0.827
M_W and M	$M_W = -0.1689 + 1.0201M$	$4.3 \le M \le 6.9$	223	0.805

be effectively used for quick conversions to M_w with little error.

This study also compares the conversion equations from the previous study (Irsyam *et al*., 2017) by conducting the analysis of the residuals between the observed and estimated M_W ($M_{W\,(obs)} - M_{W\,(est)}$) based on various magnitude types (Figures 3 and 4). In fact, the previous study only has the conversion equations for mb, M_S, and M_L. However, it is assumed that mB and M_{LV} in the previous study have the same equations for mb and M_s respectively and the generic magnitude M is equal to M_W. These residuals show how closely the estimated magnitudes match the observed ones, with zero representing a perfect match. The histograms illustrate that this study's conversions (black bars) generally cluster closer to zero, suggesting that the regression models in this study offer improved accuracy over the previous model, particularly for mB, M_L, and M_{LV}. Additionally, the scatter plots offer a closer look at the distribution of residuals for each magnitude type. This study's models are more tightly centered around zero compared to the previous study which indicate that these models achieve a balanced accuracy, minimizing both over- and underestimations across the magnitude range. This enhancement is critical for reducing errors in earthquake magnitude estimations, which can significantly impact seismic hazard assessment.

In order to estimate M_w for each event, Figure 5 presents M_W a comparison between observed and estimated using two different estimation methods. In plot (a), the estimated magnitudes are derived from the mean of available converted magnitudes and in plot (b), the estimated magnitudes are selected based on the highest R^2 from available converted magnitudes. Although the plot (b) shows a slightly better fit, it is crucial to minimize the error of magnitude conversion. Thus, we decide to use the highest R^2 method to conduct the next steps.

Smoothing Seismicity Model

The temporal distribution of earthquake magnitudes prior to and following declustering is shown in Figure 6. The beginning time-magnitude distribution of 24,315 recorded events is shown in panel (a), and the matching occurrence rate of these events is shown in panel (b). The dataset decreases substantially to 7,277 events by the declustering technique, which eliminates aftershocks and foreshocks to keep only independent mainshock events, as seen in panels (c) and (d). In order to improve the stability and dependability of the seismic hazard forecast, it is crucial to make sure that the statistical studies of the Frequency - Magnitude Distribution (FMD) that follow are based on separate seismic occurrences. Figure 7 displays the declustered events' distribution. Ad-

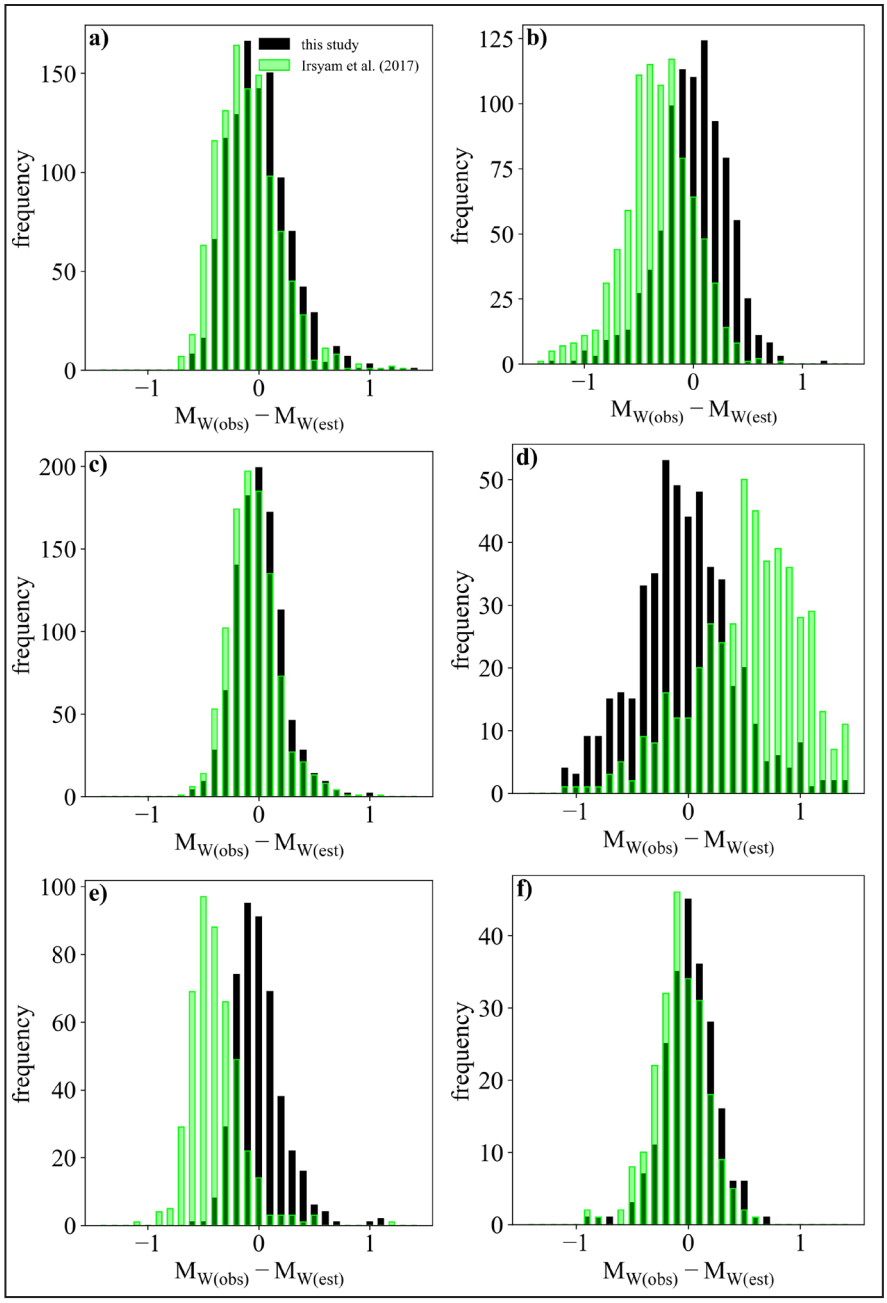

Figure 3. The histogram of residuals between this study and Irsyam *et al.* (2017).

ditionally, the temporal history of M_c from 1964 to 2024 is presented in Table 3, which supports the time-magnitude analysis in Figure 6. M_c values, which represent the lowest earthquake magnitude that can be accurately recorded, have gradually declined from 5.1 in 1964 to 2.2 in 2019. This pattern shows how seismic monitoring technology has advanced significantly over time, making it possible to identify earthquakes with smaller magnitudes.

Figure 8 expands on the spatial analysis by depicting smoothed seismicity rates across the study area, with different smoothing bandwidths (25, 50, 75, and 100 km). The maps visualize annual seismicity rates with color gradients, where green indicates lower rates and red denotes higher rates. Events are further categorized by magnitude, with smaller magnitudes represented by dots and larger events by stars. This layered approach, using varying bandwidths for Gaussian smoothing,

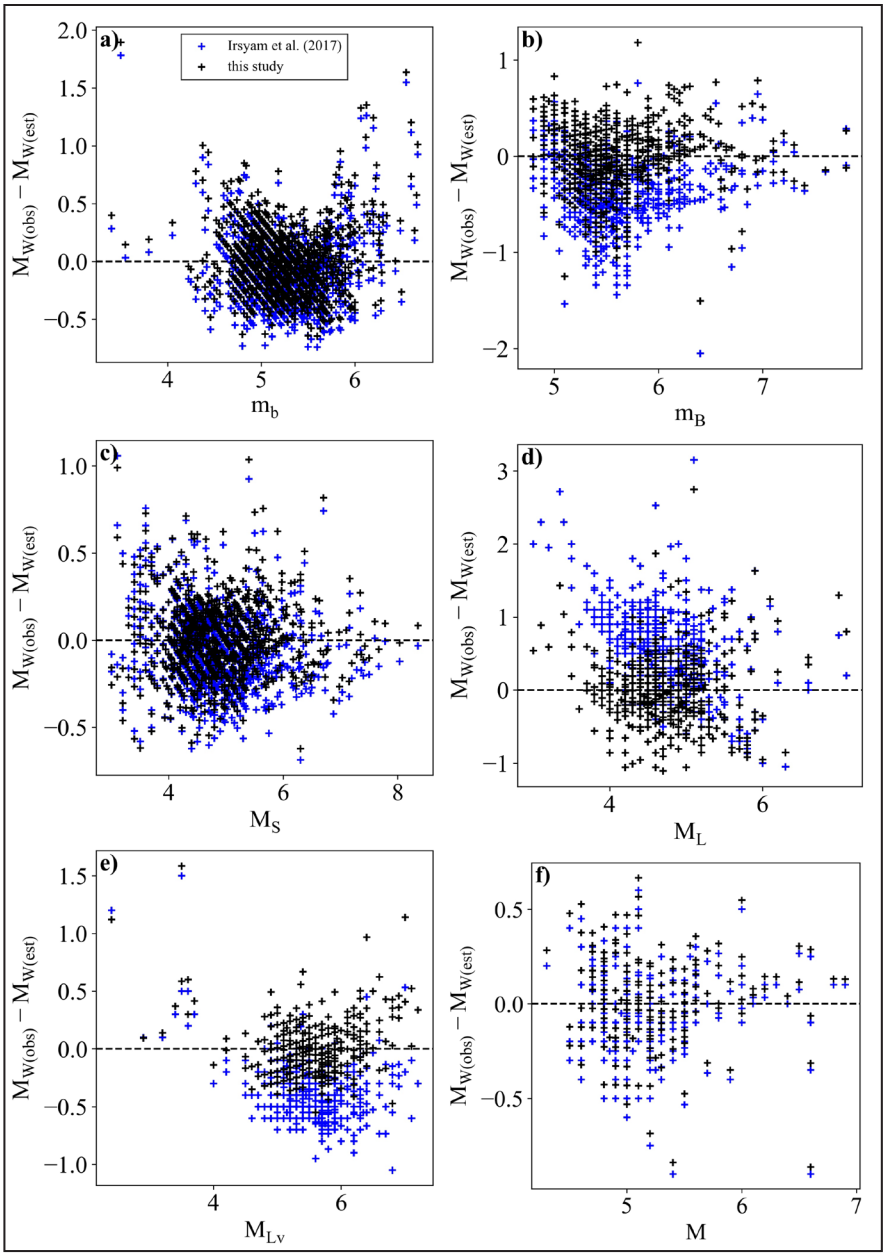

Figure 4. The plot of residuals between this study and Irsyam *et al*. (2017).

reveals how changes in spatial aggregation affect the resolution of seismic activity. The application of different bandwidths enables a detailed examination of spatial smoothing, balancing regional coverage and localized detail, which is essential for accurate hazard identification (Helmstetter and Werner, 2014; Xhafaj *et al*., 2024).

Area Source Model

Figure 9 presents FMD of declustered seismic events before 2014, demonstrating the need to accommodate two distinct trends in FMD. To accurately model these trends, we decide by selecting a weighted average of R^2 values for each scenario of cut-off magnitude, splitting the main trend into two distinct linear segments. This approach addresses the variation in seismicity rates across different magnitudes, ensuring that the regression captures both high- and low-magnitude events realistically. In Figure 10, the study area is delineated into distinct seismic source zones by considering the slip rate, fault type, and density

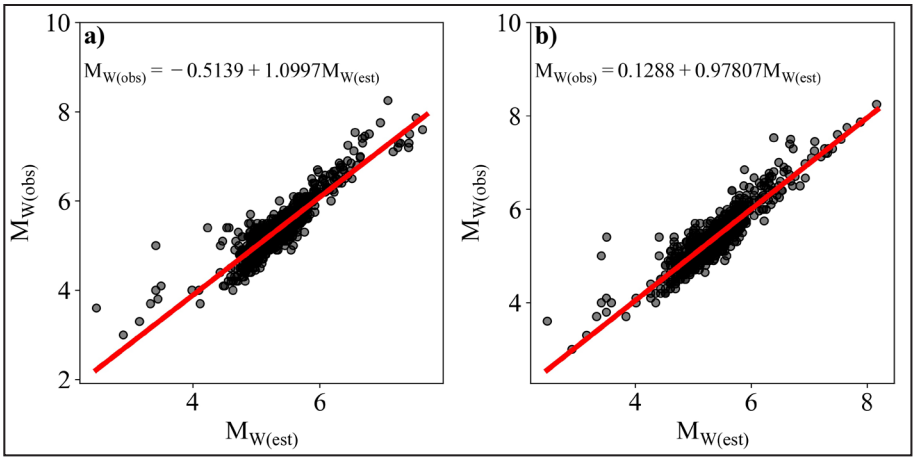

Figure 5. The plot of M_W between estimated and observed data. Red lines represent their regressions. Estimated data are obtained by: a) mean of available converted magnitudes (R^2 = 0.822) and b) selecting data based on the largest R^2 from available converted magnitudes (R^2 = 0.831).

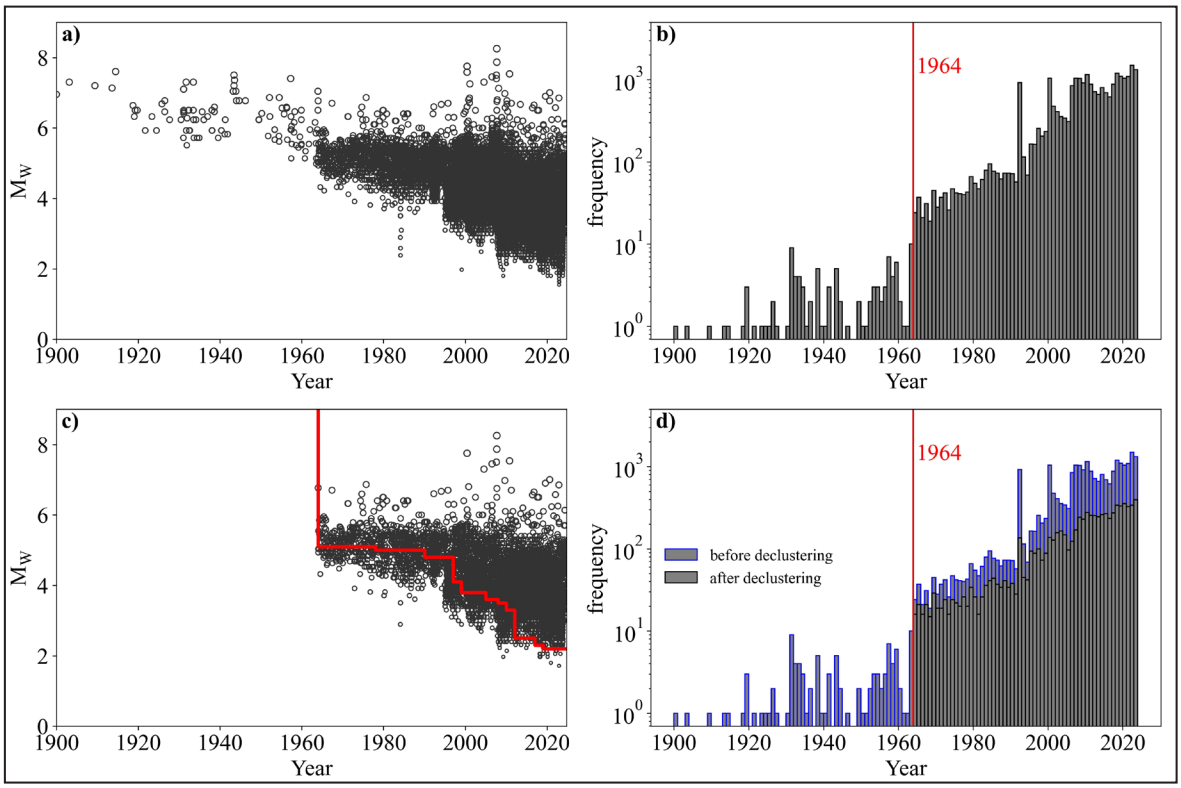

Figure 6. (a) Time-magnitude distribution and (b) event occurrences over time before declustering, with a total of 24,315 events. (c) Time-magnitude distribution with M_c and (d) event occurrences over time after declustering, with a reduced total of 7,277 events.

of recorded events. These criteria allow for targeted assessments of seismic hazard, as different regions may experience varying levels of seismic activity and tectonic settings.

Figure 11 and 12 provide further insights into FMD within the delineated area sources, using different methods for parameter estimation. Besides, Table 4 and 5 summarize the area-specific parameters derived from Figures 11 and 12, respectively. Figure 11 presents estimates for both *a* and *b* values, whereas Figure 12 estimates only the *a* values, fixing the *b* value at 1, consistent

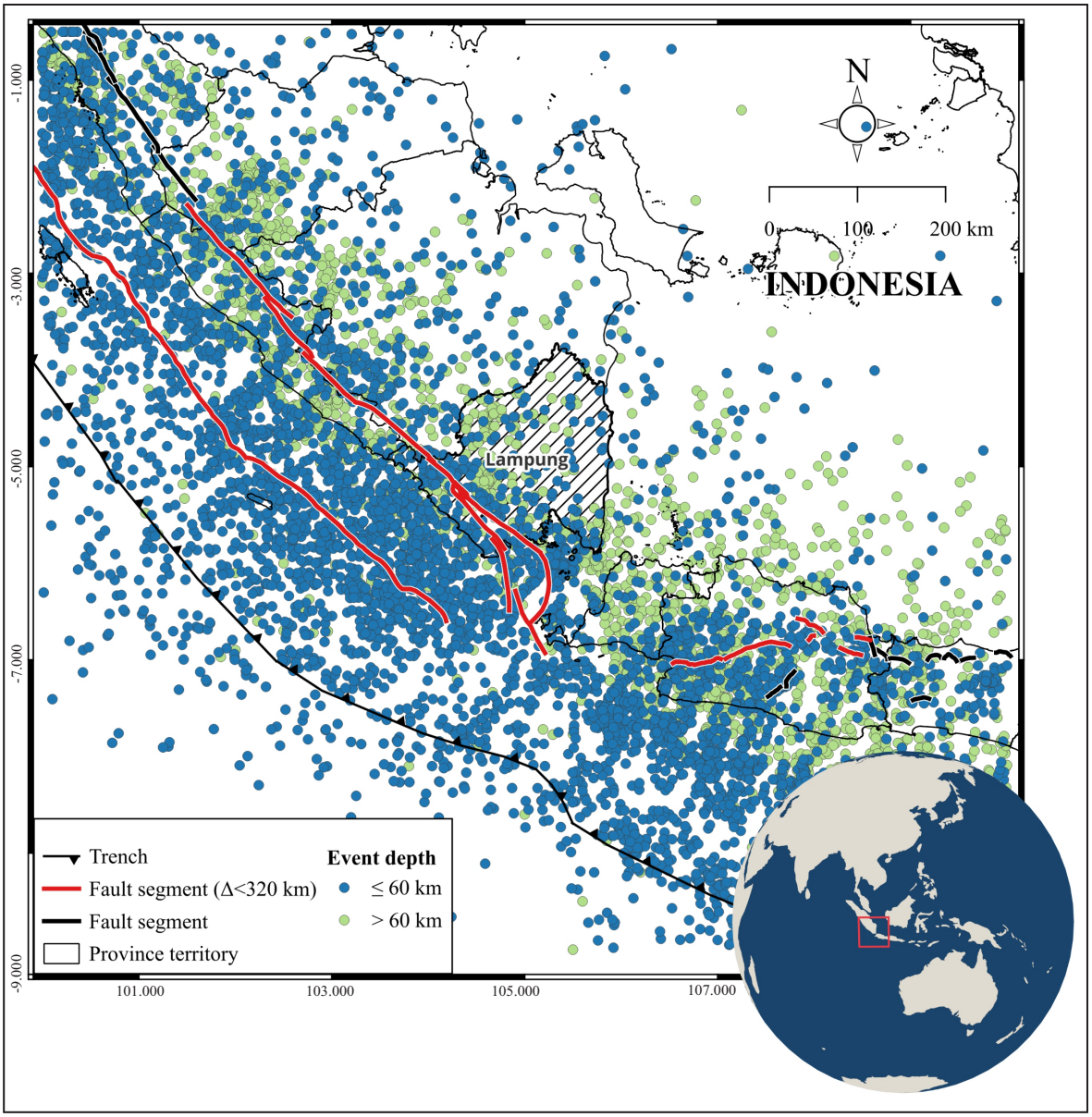

Figure 7. Declustered Earthquake Events in this study. The map displays earthquake events categorized by depth, with blue circles representing shallow events (≤ 60 km) and green circles representing deeper events (> 60 km). Key geological features are highlighted, including trenches (black lines), fault segments less than 320 km (red lines), and other fault segments (black lines). The highlighted area represents Lampung Province, a key area of study due to its seismic activity.

Table 3. Temporal Trends in Magnitude of Completeness (M_c) from 1964 to 2024

Year	1964	1978	1990	1997	1999	2005	2008	2010	2012	2017	2019
M_C	5.1	5.0	4.8	4.1	3.8	3.6	3.5	3.3	2.5	2.3	2.2

with the assumed *b* for smoothed seismicity. This approach maintains a standardized *b*-value, allowing for comparison with smoothing models. In Table 4 and 5, the selected regression types-MLE or OLS-are chosen based on the lowest standard deviation of *b* values rather than the highest R^2 values, as lower *b*-value variability provides a more stable and visually realistic model. Previous assessments in the southern Sumatra Subduction Zone, specifically across the Bengkulu, Lampung, and Sunda segments, strongly support the importance of evaluating

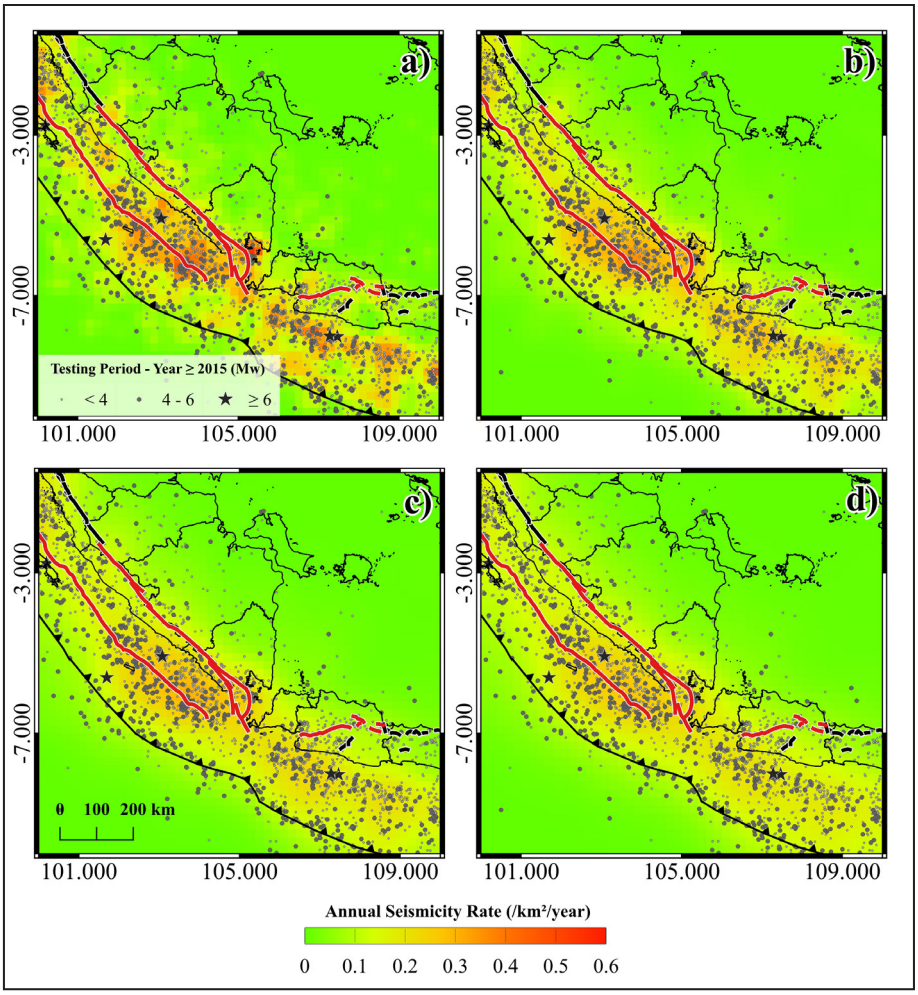

Figure 8. Smoothed Seismicity Rates (Testing Period: Events until 2014, Magnitude < 6.5). The maps display annual seismicity rates with different smoothing bandwidths: (a) 25 km, (b) 50 km, (c) 75 km, and (d) 100 km. Seismic events are categorized by magnitude, with symbols representing magnitudes < 4 (small dots), 4-6 (larger dots), and ≥ 6 (larger stars). The color scale indicates the annual seismicity rate (/km²/year), with green representing lower rates and red representing higher rates.

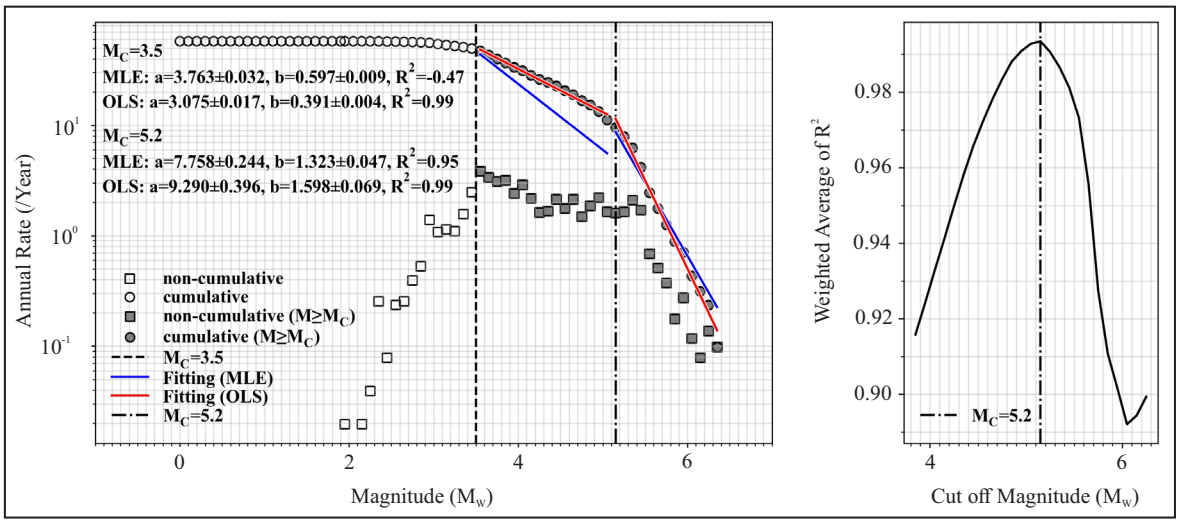

Figure 9. Left: Frequency-Magnitude distribution of declustered events with year ≤ 2014 for M_W < 6.5 and depth ≤ 60 km. Right: Decision to use M_c =5.2 as the cut-off magnitude of the two regressions (OLS).

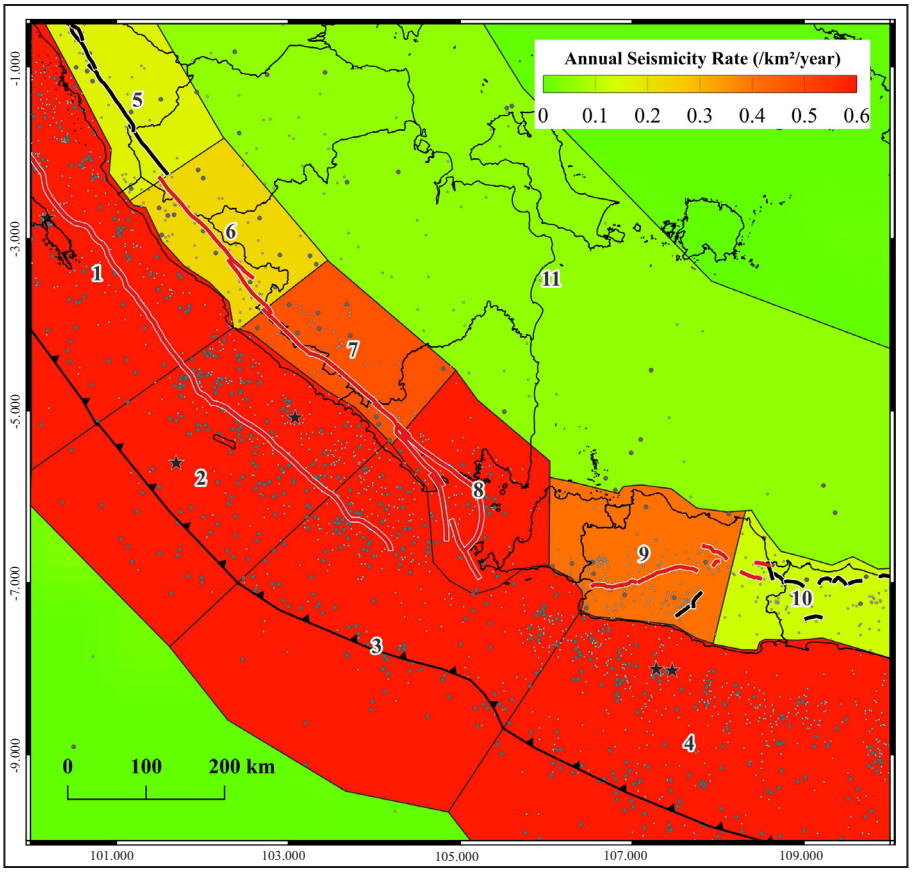

Figure 10. Seismicity Rates by Area Source in 2014 for Magnitude of Completeness (M_c) = 3.5. This map illustrates different seismic source areas in Sumatra and Java, labeled from 1 to 11, along with their respective annual seismicity rates (/km²/year). The color gradient represents varying seismicity rates, with green indicating lower rates and red indicating higher rates. The division of the region into distinct source areas allows for targeted seismic hazard assessments based on localized activity levels.

these regional seismicity parameters. Rasimeng *et al*. showed that the degree of geographical variability and high levels of stress are correlated with segment-specific differences in b-values (ranging from 0.69 to 0.83). Analyzing these differences is also crucial since they are important markers for estimating the likelihood and duration of future large-magnitude earthquakes in those specific areas.

Model Validation

The validation of the area source and smoothing seismicity models is rigorously evaluated using the Molchan diagram presented in Figure 13. By comparing the performance of various smoothing bandwidths and area source models, the Molchan diagram quantifies the models' skill in capturing real earthquake occurrences within the defined study period, with ASS used as a key metric for evaluation. In the Molchan diagram, a curve closer to the bottom left corner indicates a higher predictive skill, as it suggests a model can accurately forecast events. In general, the smoothed seismicity models exhibit better performance than the area source model, demonstrating greater sensitivity to localized seismicity variations. This sensitivity is quantitatively supported by the ASS values summarized in Table 6, where smoothed seismicity models achieve consistently higher scores (0.81) compared to the area source model (0.7). Moreover, the smoothed seismicity models show competitive performance across different bandwidths, emphasizing the importance of selecting an optimal bandwidth-such as 50 km-for stable and reliable hazard forecasting.

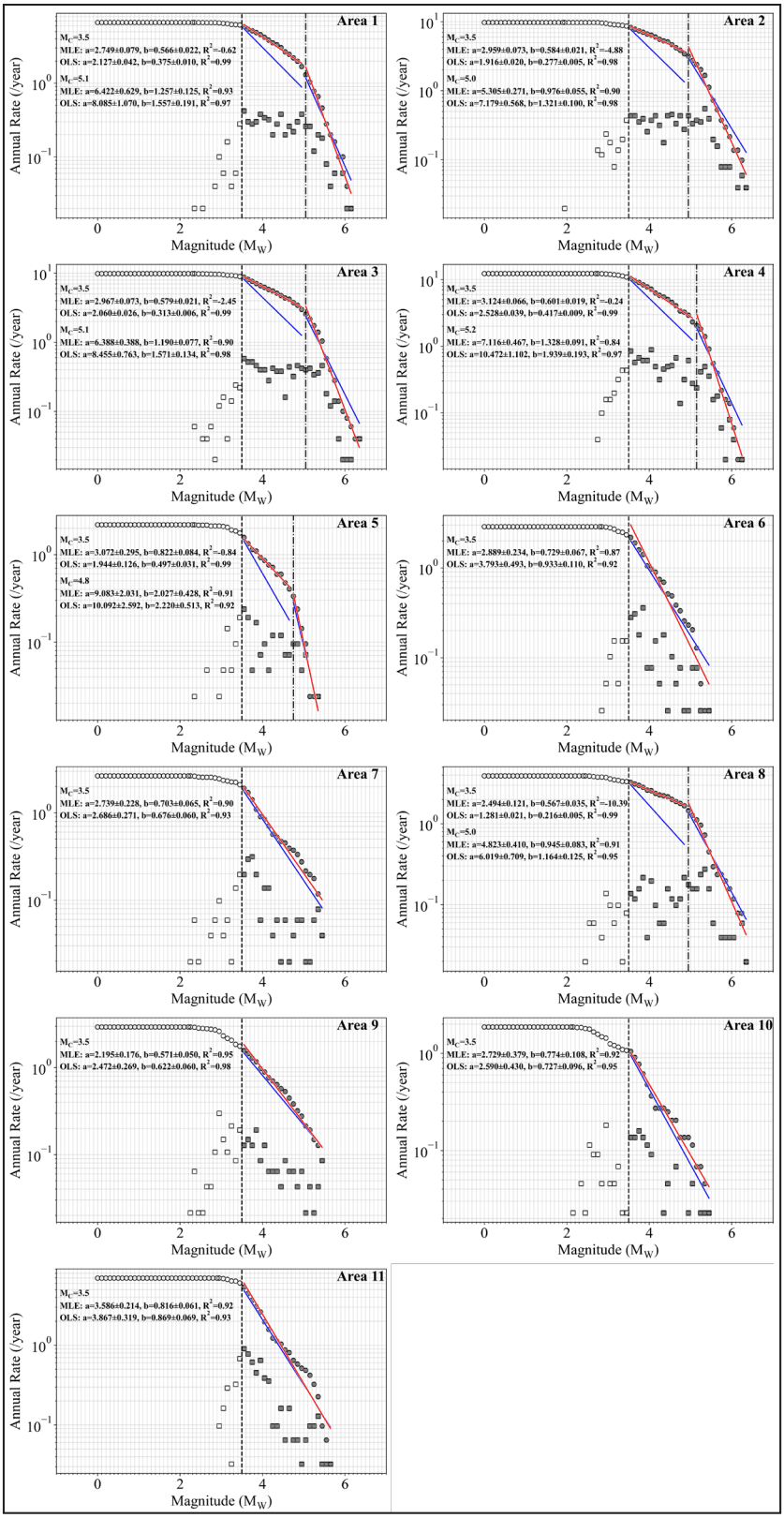

Figure 11. Frequency-Magnitude distributions of declustered seismic events (year ≤ 2014, M_W<6.5, and depth ≤ 60 km) for each area source (Area 1 to Area 8). Each plot shows the annual rate of events as a function of magnitude, with maximum likelihood estimates (MLE) and ordinary least squares (OLS) fitted lines represented in red and blue, respectively. The statistical parameters (e.g. *a*- and *b*-values, R^2) for each area are displayed on the plots, providing insights into the seismicity characteristics across different regions.

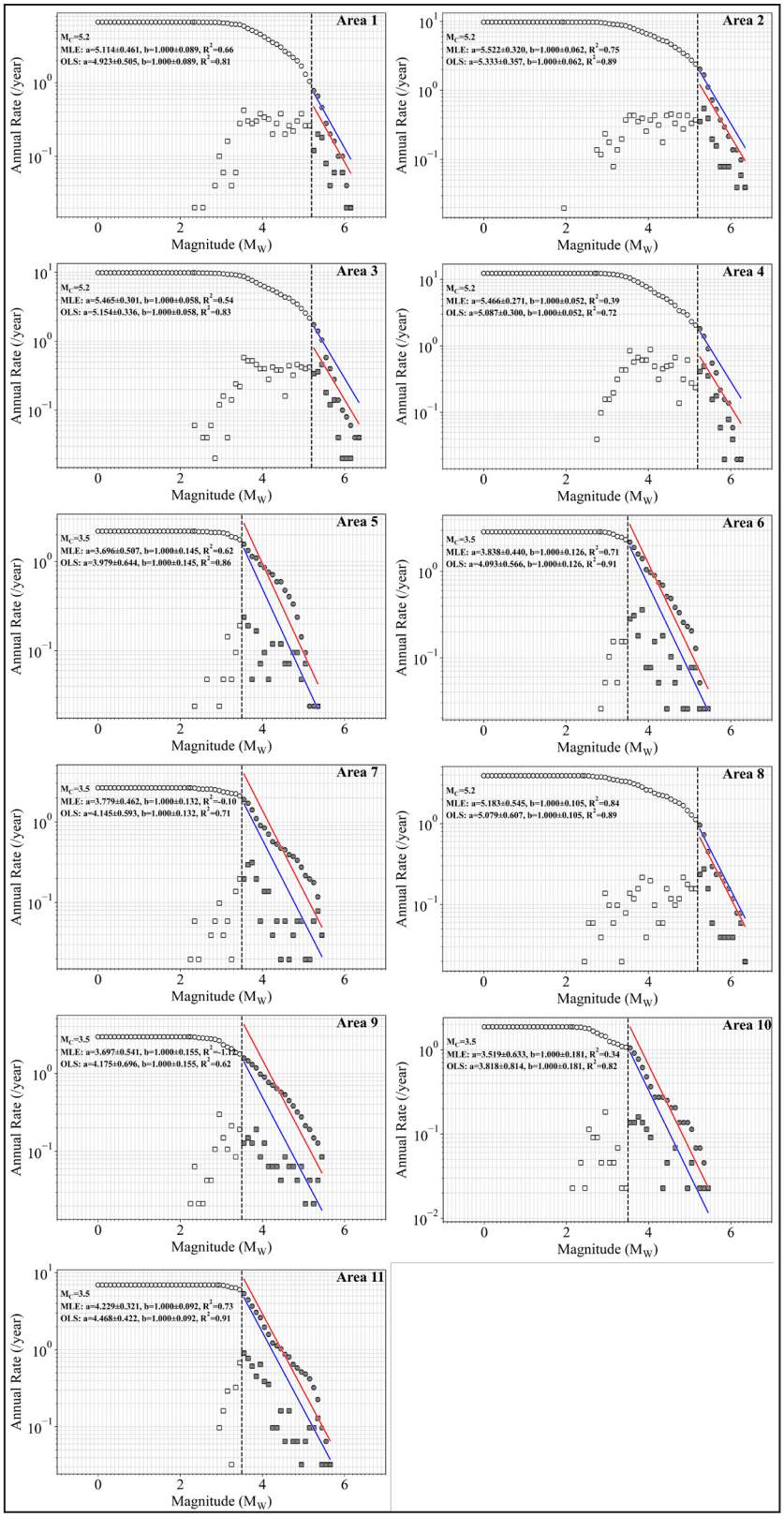

Figure 12. Frequency-Magnitude distributions of declustered seismic events (year ≤ 2014, M_W <65, and depth ≤ 60 km) across eight area sources (Area 1 to Area 8), assuming a *b*-value of 1. Each plot presents the annual rate of events as a function of magnitude, with maximum likelihood estimates (MLE) and ordinary least squares (OLS) fits shown in red and blue, respectively. Statistical parameters, including *a* - and *b*-values, R^2 coefficients, are noted on each plot, highlighting variations in seismicity among different regions.

Table 4. Characteristics of area sources, showing seismicity parameters and descriptions for each area. Parameters include area size, *a* - and *b* -Values (with standard deviations), R^2 values, regression type, and the calculated annual seismicity rate per square kilometer. All areas assume a magnitude of completeness M_c=3.5. The regression type OLS or MLE is selected based on the lowest σ_b.

Area No.	Area (km²)	*a* (/year)	*b*	R^2	Regression Type	Annual Seismicity Rate (/km²/year)
1	74,171.1	2.127 ± 0.042	0.375 ± 0.010	0.99	OLS	0.0018062
2	98,873.4	1.916 ± 0.020	0.277 ± 0.005	0.98	OLS	0.0008335
3	131,583.0	2.060 ± 0.026	0.313 ± 0.006	0.99	OLS	0.0008726
4	132,717.1	2.528 ± 0.039	0.417 ± 0.009	0.99	OLS	0.0025414
5	30,163.4	1.944 ± 0.126	0.497 ± 0.031	0.99	OLS	0.0029142
6	29,939.7	2.889 ± 0.234	0.729 ± 0.067	0.87	MLE	0.0258674
7	29,681.7	2.686 ± 0.271	0.676 ± 0.060	0.93	OLS	0.0163498
8	35,737.5	1.281 ± 0.021	0.216 ± 0.005	0.99	OLS	0.0005344
9	37,316.9	2.195 ± 0.176	0.571 ± 0.050	0.95	MLE	0.0041985
10	25,746.3	2.590 ± 0.430	0.727 ± 0.096	0.95	OLS	0.0151107
11	307,656.5	3.586 ± 0.214	0.816 ± 0.061	0.92	MLE	0.0125295

Table 5. Characteristics of area sources assuming b = 1, showing seismicity parameters and descriptions for each area. Parameters include area size, magnitude of completeness (M_c), *a*-values (with standard deviations), R^2 values, regression type, and annual seismicity rate per square kilometer. The regression type OLS or MLE is selected based on the lowest σ_b.

Area No.	Area (km²)	M_c	*a* (/year)	*b*	R^2	Regression Type	Annual Seismicity Rate (/km²/year)
1	74,171.1	5.2	4.923 ± 0.505	1.000 ± 0.089	0.81	OLS	1.1291845
2	98,873.4	5.2	5.333 ± 0.357	1.000 ± 0.062	0.89	OLS	2.1773119
3	131,583.0	5.2	5.154 ± 0.336	1.000 ± 0.058	0.83	OLS	1.0834284
4	132,717.1	5.2	5.087 ± 0.300	1.000 ± 0.052	0.72	OLS	0.9206043
5	30,163.4	3.5	3.696 ± 0.507	1.000 ± 0.145	0.62	MLE	0.1646342
6	29,939.7	3.5	3.838 ± 0.440	1.000 ± 0.126	0.71	OLS	0.2300129
7	29,681.7	3.5	4.145 ± 0.593	1.000 ± 0.132	0.71	OLS	0.4704475
8	35,737.5	5.2	5.079 ± 0.607	1.000 ± 0.105	0.89	OLS	3.3564126
9	37,316.9	3.5	4.175 ± 0.696	1.000 ± 0.155	0.62	OLS	0.4009544
10	25,746.3	3.5	3.519 ± 0.633	1.000 ± 0.181	0.34	MLE	0.1283172
11	307,656.5	3.5	4.229 ± 0.321	1.000 ± 0.092	0.73	MLE	0.0550724

Discussion

In this study, using magnitude conversion equations from prior research without verification may not yield accurate results for this specific region. The previous equations may not accurately represent the unique seismic characteristics of the study area. To address this concern, the study proposes verifying the suitability of these equations. When uncertainty remains, regression analysis can be performed to generate new equations tailored to the region, improving the reliability of magnitude estimations for hazard assessments. Figures 2 and 3 in the study illustrate various magnitude conversion relationships, comparing them with past models to highlight potential improvements in estimation accuracy for this region.

Although MLE is generally favored for estimating linear regressions within FMD, OLS can serve as a useful comparative approach in this study. Notably, OLS sometimes demonstrates a better visual fit with observed data, potentially enhancing interpretability in certain cases. In the study, both MLE and OLS regression methods are used, as shown in Figures 11 and 12, where each approach's outcomes are analyzed to determine which yields the most stable estimates of seismic parameters within different segmented areas. This

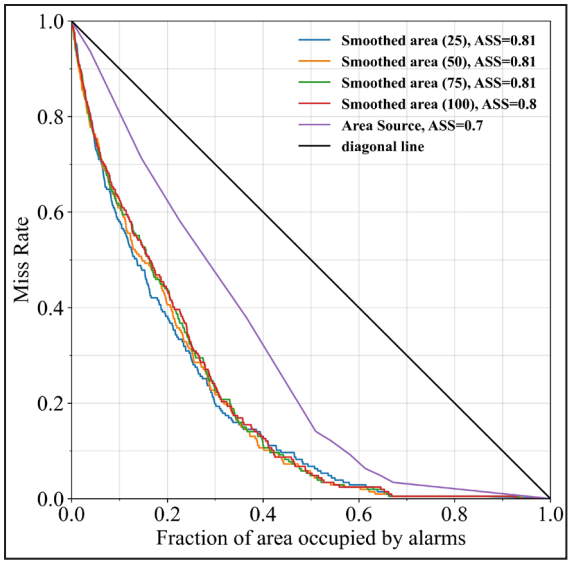

Figure 13. Molchan diagram comparing the performance of different seismic hazard models, illustrated by smoothed areas at various scales (25, 50, 75, and 100) and an area source model. The diagram shows the trade-off between the miss rate and the fraction of area occupied by alarms, with Alarm Skill Score (ASS) values indicating model effectiveness. The diagonal line represents random prediction.

Table 6. Model performance comparison between smoothed seismicity and area source models based on the Area Skill Score (ASS)

Model Type	Smoothing Bandwidth (km)	Area Skill Score (ASS)
Smoothed Area	25	0.81
Smoothed Area	50	0.81
Smoothed Area	75	0.81
Smoothed Area	100	0.8
Area Source	N/A	0.7

comparative analysis provides insight into the potential for variability in regression performance across different models.

Area-source modeling and seismicity smoothing are then employed as complementary approaches. The area-source models capture broad trends within defined geographic regions, while smoothed seismicity models apply varying bandwidths to highlight seismic hazard patterns across space. For model validation, the Molchan diagram serves as a critical tool in assessing the predictive accuracy of both area source and smoothed seismicity models (Figure 13). By plotting the fraction of observed seismic events that fall within forecasted areas against the fraction of the study area marked as "alarmed," the Molchan diagram provides a quantitative measure of each model's effectiveness. A model with curves closer to the bottom-left corner indicates higher predictive skill, as it accurately captures events within a minimal alarmed area. In addition, ASS has proven effective in evaluating the accuracy of seismic models, where a higher ASS indicates a model's increased accuracy in capturing observed seismicity patterns. In particular, smaller bandwidths reveal more granular insights into high-seismicity areas, which are crucial for site-specific hazard assessments, while larger bandwidths yield broader trends that are helpful for regional planning. In comparing variant bandwidths within smoothed seismicity models, bandwidths of 25, 50, and 75 exhibit competitive ASS values. However, a notable trade-off emerges below and above the 0.4 threshold for the "Fraction of area occupied by alarms," with discrepancies in miss rate observable in Figure 13. Of these options, a 50 km bandwidth achieves a more stable curve, minimizing the influence of this trade-off and ensuring consistent performance in forecasting seismic events. This finding underscores the importance of bandwidth selection in producing stable and reliable models for seismic hazard assessment.

The study's multi-faceted approach to seismic hazard assessment in Lampung offers a robust framework for understanding and mitigating seismic risks in the region. By combining rigorous magnitude conversion, declustering, spatial smoothing, and area-source modeling techniques, it develops a comprehensive picture of local seismicity. Such an approach is critical for informed decision-making, providing a valuable resource for both local authorities and regional planners tasked with designing infrastructure and safety protocols that can withstand potential seismic impacts. This methodology demonstrates how a detailed, region-specific analysis can enhance the reliability of seismic hazard assessments, ultimately contributing to more resilient and disaster-prepared communities.

Conclusions

This study provides an enhanced seismic hazard assessment for the Lampung region through a refined approach to magnitude conversion, seismicity smoothing, and area-source modeling. By adjusting magnitude conversion equations, we ensure that the models are regionally relevant and accurate.

The comparison of MLE and OLS for frequency-magnitude distribution reveals that, although MLE is generally preferred, OLS can yield a visually closer fit with observed data in specific instances, making it a useful complementary method.

Applying Gaussian smoothing with variant bandwidths demonstrates that a 50 km bandwidth offers a stable and high-performing model, as confirmed by the ASS and Molchan diagram, which emphasize the predictive reliability of smoothed seismicity models.

Dividing the study area into separate seismic zones based on tectonic characteristics and event density improves the detail of the hazard assessment, allowing high-seismicity regions to be accurately identified.

Overall, the study's combination of region-specific magnitude conversion, smoothing seismicity, and shallow area source modeling produces a comprehensive framework for seismic hazard preparedness. These insights provide a robust foundation for informed decision-making, facilitating effective disaster risk mitigation and resilient infrastructure planning in Lampung.

Acknowledgments

This work was financially supported by an internal grant from Institut Teknologi Sumatera for early-career lecturers, under contract No.1539ci/IT9.2.1/PT.01.03/2024. I would like to express my sincere gratitude to the research team and all collaborators for their valuable contributions throughout the project.

References

Abe, K., 1981. Magnitudes of large shallow earthquakes from 1904 to 1980. *Physics of the Earth and Planetary Interiors*, 27, p.72-92. DOI: 10.1016/0031-9201(81)90088-1

Baker, J., Bradley, B., and Stafford, P., 2022. *Seismic Hazard and Risk Analysis*, New edition. ed. Cambridge University Press, Cambridge New York.

Bellier, O., Sébrier, M., Pramumijoyo, S., Beaudouin, Th., Harjono, H., Bahar, I., and Forni, O., 1997. Paleoseismicity and seismic hazard along the Great Sumatran Fault (Indonesia). *Journal of Geodynamics, Paleoseismology: Understanding Past Earthquakes Using Quaternary Geology*, 24, p.169-183. DOI: 10.1016/S0264-3707(96)00051-8

Bradley, K.E., Feng, L., Hill, E.M., Natawidjaja, D.H., and Sieh, K., 2017. Implications of the diffuse deformation of the Indian Ocean lithosphere for slip partitioning of oblique plate convergence in Sumatra. *Journal of Geophysical Research: Solid Earth*, 122, p.572-591. DOI: 10.1002/2016JB013549

Collings, R., Rietbrock, A., Lange, D., Tilmann, F., Nippress, S., and Natawidjaja, D., 2013. Seismic anisotropy in the Sumatra subduction zone. *Journal of Geophysical Research: Solid Earth*, 118, p.5372-5390. DOI: 10.1002/jgrb.50157

Frankel, A., 1995. Mapping Seismic Hazard in the Central and Eastern United States. *Seismological Research Letters*, 66, p.8-21. DOI: 10.1785/gssrl.66.4.8

Gardner, J.K. and Knopoff, L., 1974. Is the sequence of earthquakes in Southern California, with aftershocks removed, Poissonian? *Bulletin of the Seismological Society of America*, 64, p.1363-1367. DOI: 10.1785/BSSA0640051363

Haifani, A.M., Setiadipura, T., and Prakoso, W.A., 2026. Application of the Simple Multi-Attribute Rating Technique (SMART) for Selecting Compatible Earthquake Time Series in Liquefaction Analysis Support: Case Study in Serpong, Tangerang, Indonesia. *Indonesian*

Journal on Geoscience, 13 (1), p.57-76. DOI: 10.17014/ijog.13.1.57-76

Hanks, T.C. and Kanamori, H., 1979. A moment magnitude scale. *Journal of Geophysical Research: Solid Earth*, 84, p.2348-2350. DOI: 10.1029/JB084iB05p02348

Haridhi, H.A., Huang, B.-S., Wen, K.-L., Denzema, D., Prasetyo, R.A., and Lee, C.-S., 2018. A study of large earthquake sequences in the Sumatra subduction zone and its possible implications. *Terrestrial, Atmospheric and Oceanic Sciences*, 29, p.635-652. DOI: 10.3319/TAO.2018.08.22.01

Helmstetter, A. and Werner, M.J., 2014. Adaptive Smoothing of Seismicity in Time, Space, and Magnitude for Time-Dependent Earthquake Forecasts for California. *Bulletin of the Seismological Society of America*, 104, p.809-822. DOI: 10.1785/0120130105

Hu, Y., Li, Y., and Xu, M., 2026. The Trans-Sumatra Toll Road and Economic Geography in Indonesia. *Journal of Economic Geography*, Article lbag039. DOI: 10.1093/jeg/lbag039

International Seismological Centre, 2024. *On-line Bulletin*. DOI: 10.31905/D808B830

Irsyam, M., Cummins, P.R., Asrurifak, M., Faizal, L., Natawidjaja, D.H., Widiyantoro, S., Meilano, I., Triyoso, W., Rudiyanto, A., Hidayati, S., Ridwan, M., Hanifa, N.R., and Syahbana, A.J., 2020. Development of the 2017 national seismic hazard maps of Indonesia. *Earthquake Spectra*, 36, p.112-136. DOI: 10.1177/8755293020951206

Irsyam, M., Widiyantoro, S., Natawidjaja, D.H., Meilano, I., Rudyanto, A., Hidayati, S., Triyoso, W., Hanifa, N.R., Djarwadi, D., Faizal, L., and Sunarjito, 2017. *Peta Sumber dan Bahaya Gempa Indonesia Tahun 2017*. Pusat Penelitian dan Pengembangan Perumahan dan Pemukiman Badan Penelitian dan Pengembangan Kementerian Pekerjaan Umum dan Perumahan Rakyat.

Kadirioğlu, F. and Kartal, R., 2016. The new empirical magnitude conversion relations using an improved earthquake catalogue for Turkey and its near vicinity (1900-2012). *Turkish Journal of Earth Sciences*, 25, p.300-310. DOI: 10.3906/yer-1511-7

Kagan, Y.Y. and Jackson, D.D., 1994. Long-term probabilistic forecasting of earthquakes. *Journal of Geophysical Research: Solid Earth*, 99, p.13685-13700. DOI: 10.1029/94JB00500

Lamichhane, K., Bhattarai, S., Rajan, K.C., Sharma, K., and Pokhrel, R., 2025. State-of-the-art review of probabilistic seismic hazard analysis in Nepal: Status, challenges, and recommendations. *Geoenvironmental Disasters*, 12 (1), Article 15. DOI: 10.1186/s40677-025-00320-0

Mandal, H.S., Shukla, A.K., Khan, P.K., and Mishra, O.P., 2013a. A new insight into probabilistic seismic hazard analysis for central india. *Pure and Applied Geophysics*, 170 (12), p.2139-2161. DOI: 10.1007/s00024-013-0666-x

McCaffrey, R., 2009. The Tectonic Framework of the Sumatran Subduction Zone. *Annual Review of Earth and Planetary Sciences*, 37, p.345-366. DOI: 10.1146/annurev.earth.031208.100212

Molchan, G.M., 1991. Structure of optimal strategies in earthquake prediction. *Tectonophysics*, 193, p.267-276. DOI: 10.1016/0040-1951(91)90336-Q

Molchan, G.M., 1990. Strategies in strong earthquake prediction. *Physics of the Earth and Planetary Interiors*, 61, p.84-98. DOI: 10.1016/0031-9201(90)90097-H

Molchan, G.M. and Kagan, Y.Y., 1992. Earthquake prediction and its optimization. *Journal of Geophysical Research: Solid Earth*, 97, p.4823-4838. DOI: 10.1029/91JB03095

Natawidjaja, D.H., Sieh, K., Chlieh, M., Galetzka, J., Suwargadi, B.W., Cheng, H., Edwards, R.L., Avouac, J.-P., and Ward, S.N., 2006. Source parameters of the great Sumatran megathrust earthquakes of 1797 and 1833 inferred from coral microatolls. *Journal of Geophysical Research: Solid Earth*, 111. DOI: 10.1029/2005JB004025

Pesicek, J.D., Thurber, C.H., Widiyantoro, S., Engdahl, E.R., and DeShon, H.R., 2008. Complex slab subduction beneath northern

Sumatra. *Geophysical Research Letters*, 35 (20), L20303. DOI: 10.1029/2008GL035262

Petersen, M.D., Dewey, J., Hartzell, S., Mueller, C., Harmsen, S., Frankel, A.D., and Rukstales, K., 2004. Probabilistic seismic hazard analysis for Sumatra, Indonesia and across the Southern Malaysian Peninsula. *Tectonophysics, Strong Ground Motion, Earthquake Hazard and Risk in Alpine-Himalayan and Pacific Regions*, 390, p.141-158. DOI: 10.1016/j.tecto.2004.03.026

Qiu, Q. and Chan, C.-H., 2019. Coulomb stress perturbation after great earthquakes in the Sumatran subduction zone: Potential impacts in the surrounding region. *Journal of Asian Earth Sciences*, 180, p.103869. DOI: 10.1016/j.jseaes.2019.103869

Rasimeng, S., Helmi, M., Tugiyono, T., and Suharno, S., 2022. Fractal Dimension Analysis and Earthquake Repeated Period Estimation in the Southern Part of Sumatra Subduction Zone (Bengkulu-Lampung-Sunda Segment). *Indonesian Journal on Geoscience*, 9 (3), p.383-394. DOI: 10.17014/ijog.9.3.383-394

Richter, C.F., 1958. *Elementary Seismology*, Presumed First Edition. ed. W H Freeman & Co.

Savran, W.H., Werner, M.J., Schorlemmer, D., and Maechling, P.J., 2024. *pyCSEP - Tools for Earthquake Forecast Developers*. DOI: 10.5281/zenodo.10620937

Sieh, K. and Natawidjaja, D., 2000. Neotectonics of the Sumatran fault, Indonesia. *Journal of Geophysical Research: Solid Earth*, 105, p.28295-28326. DOI: 10.1029/2000JB900120

Singh, S.C., Carton, H., Tapponnier, P., Hananto, N.D., Chauhan, A.P.S., Hartoyo, D., Bayly, M., Moeljopranoto, S., Bunting, T., Christie, P., Lubis, H., and Martin, J., 2008. Seismic evidence for broken oceanic crust in the 2004 Sumatra earthquake epicentral region. *Nature Geoscience*, 1, p.777-781. DOI: 10.1038/ngeo336

Subarya, C., Chlieh, M., Prawirodirdjo, L., Avouac, J.-P., Bock, Y., Sieh, K., Meltzner, A.J., Natawidjaja, D.H., and McCaffrey, R., 2006. Plate-boundary deformation associated with the great Sumatra–Andaman earthquake. *Nature*, 440, p.46-51. DOI: 10.1038/nature04522

Triyoso, W. and Sahara, D.P., 2021. Seismic Hazard Function Mapping Using Estimated Horizontal Crustal Strain Off West Coast Northern Sumatra. *Frontiers in Earth Science*, 9, Article 558923. DOI: 10.3389/feart.2021.558923

Triyoso, W., Suwondo, A., Yudistira, T., and Sahara, D.P., 2020. Seismic Hazard Function (SHF) study of coastal sources of Sumatra Island: SHF evaluation of Padang and Bengkulu cities. Geoscience Letters, 7, Article 2. DOI: 10.1186/s40562-020-00151-x

USNRC, 2007. *Regulatory Guide 1.208: A Performance-based Approach to Define the Site-specific Earthquake Ground Motion*. U.S. Nuclear Regulatory Commission.

Weichert, D.H., 1980. Estimation of the earthquake recurrence parameters for unequal observation periods for different magnitudes. *Bulletin of the Seismological Society of America*, 70, p.1337-1346. DOI: 10.1785/BSSA0700041337

Wiemer, S., García-Fernández, M., and Burg, J.-P., 2009. Development of a seismic source model for probabilistic seismic hazard assessment of nuclear power plant sites in Switzerland: the view from PEGASOS Expert Group 4 (EG1d). *Swiss Journal of Geosciences*, 102, p.189-209. DOI: 10.1007/s00015-009-1311-7

Willemann, R.J. and Storchak, D.A., 2001. Data Collection at the International Seismological Centre. *Seismological Research Letters*, 72, p.440-453. DOI: 10.1785/gssrl.72.4.440

Xhafaj, E., Chan, C.-H., and Ma, K.-F., 2024. Earthquake forecasting model for Albania: the area source model and the smoothing model. *Natural Hazards and Earth System Sciences*, 24, p.109-119. DOI: 10.5194/nhess-24-109-2024

Zechar, J.D. and Jordan, T.H., 2010. The Area Skill Score Statistic for Evaluating Earthquake Predictability Experiments. *Pure and Applied Geophysics*, 167, p.893-906. DOI: 10.1007/s00024-010-0086-0

Zechar, J.D. and Jordan, T.H., 2008. Testing alarm-based earthquake predictions. *Geophysical Journal International*, 172, p.715-724. DOI: 10.1111/j.1365-246X.2007.03676.x